Reacting Mixing-Layer Computations in a Simulated Turbine-Stator Passage

Felix Cheng,* Feng Liu,† and William A. Sirignano‡
University of California, Irvine, Irvine, California 92697-3975

Mixing layers composed of gaseous fuel and oxidizer streams with and without chemical reactions are studied by performing two-dimensional numerical simulations. Various channels are considered. The mixing layer in the unidirectional (straight) channel is subjected to an imposed streamwise acceleration, whereas the mixing layer in the curved channel is subjected to both transverse and streamwise accelerations. The flow accelerates from low subsonic speed to low supersonic speed for all cases considered. In this paper, we focus on the development of the mixing layer from laminar flow to the transition regime. The full Navier–Stokes equations coupled with multiple-species equations and the energy equations with chemical reactions are solved using a finite difference numerical scheme. The effects of turning are investigated on two different flow configurations: one has faster and lighter airstream on the outside of the curve and slower and heavier fuel stream on the inside of the curve; the other configuration is the inverse of the previous one. Mixing layers in a turbinelike passage are also studied.

I. Introduction

DESIGNERS of jet engines are attempting to increase the thrust-to-weight ratio and to widen the range of engine operation. Because the flow in a turbine passage is accelerating and power is extracted from the flow, it is possible to add heat without increasing the flow temperature beyond the turbine-blade material limit. Sirignano and Liu [1,2] show by thermodynamic analysis that the thrust of aircraft turbojet and turbofan engines can be increased significantly with little increase in fuel consumption by intentionally burning fuel in the turbine stages. For the ground-based gas turbine, improvement has been found in power, weight, and efficiencies [1]. Mixing and exothermic chemical reaction in the accelerating flow through the turbine passage offer an opportunity for a major technological improvement. The gas turbine engine is not the only potential application for this technology. The reduction in peak temperature due to acceleration results in the promise of reduced pollutant formation and reduced heat transfer loss in many other combustion applications.

The geometry of the turbine passage is rather complex. To simplify the problem while retaining the major physics in the present study, we create a model problem in this paper in which mixing layers of fuel and oxidizer streams going through straight and curved channels with imposed streamwise pressure gradients are studied. Both nonreacting and reacting mixing layers are considered. The nonreacting cases primarily serve as the base cases; the main focuses are on the reacting mixing layers. We focus on the fundamental physics, such as the effects of streamwise and transverse accelerations on the instability and the chemical reactions in the reacting, accelerating mixing layers.

There has been little previous research on steady-state multidimensional flows with mixing and chemical reactions in the presence of strong pressure gradients. Research has been done on high-speed, nonaccelerating, reacting flows. A comprehensive literature review was done by Sirignano and Kim [3]. In that paper, they also obtained similarity solutions for laminar, two-dimensional, mixing, reacting, and nonreacting layers with a favorable pressure gradient in the primary flow direction. Fang et al. [4] extended that study to mixing layers with arbitrary pressure gradients by using a finite difference method for the boundary-layer equations. The influence of pressure gradient, initial temperature, initial pressure, initial velocity, and transport properties was studied. Mehring et al. [5] performed a numerical study on a reacting, turbulent, and accelerating mixing layer based on the laminar boundary-layer calculations by Fang et al. [4]. Cai et al. [6] developed a finite volume method for solving the two-dimensional, compressible, Favre-averaged Navier–Stokes equations with chemical reactions using the Baldwin–Lomax turbulence model.

The steady-state calculations provide important insight into the fundamental physics of multidimensional mixing layers with chemical reactions and strong pressure gradients. However, they are unable to capture the unsteady developments in which the flows evolve from laminar conditions to turbulence. Motivated by this, the primary objective of this paper is to investigate the initial developments of the two-dimensional, reacting, accelerating mixing layers from the laminar stage to the early transitional stage.

The nonreacting mixing layers going through the curved channel are subjected to three types of instability: Kelvin–Helmholtz (K-H), centrifugal, and Rayleigh–Taylor (R-T) instabilities. K-H instability occurs in a shear layer, and has been studied extensively by experiments, stability analyses, and numerical analyses (see Ho and Huerre [7]). For a planar shear layer, the 2-D K-H modes are more unstable than the 3-D modes in the linear stage or in the early stage of transition. Experimental studies by Winant and Browand [8] show that, at the early stage of transition, the development of the mixing layer is dominated by large-scale, two-dimensional spanwise vortices that arise from the K-H instability. In highly turbulent mixing layers, the development of the three-dimensional streamwise vortices become significant. Numerical simulations of three-dimensional, temporally evolving plane mixing layers were performed by Rogers and Moser [9,10]. Infinitesimal three-dimensional disturbances were initially imposed. Spanwise vorticity rolled up into corrugated spanwise rollers, and predominantly streamwise rib vortices developed in the braid region between the spanwise rollers. The development of three-dimensionality, the nonlinear evolution of three-dimensional disturbances with spanwise vortices during pairings, and the transition mechanisms were studied in detail. Although the development of three-dimensional structures is absent in our two-dimensional study, we

*Research Assistant, Department of Mechanical and Aerospace Engineering. Member AIAA.

†Professor, Department of Mechanical and Aerospace Engineering. Associate Fellow AIAA.

‡Professor, Department of Mechanical and Aerospace Engineering. Fellow AIAA.

focus on the early stages of transition, which is dominated by a 2-D mechanism.

Centrifugal instability [11] in a curved shear layer is caused by the centrifugal force. Depending on the velocity distribution across the curved shear layer, the centrifugal force could have a stabilizing or destabilizing effect. For an inviscid swirling flow, Rayleigh [11] found that a necessary and sufficient condition for stability to axisymmetric disturbances is that the square of the circulation does not decrease with increasing radius anywhere. For an unstable curved shear layer (such as a shear layer with faster fluid on the inside of the curve), a 3-D unstable mode associated with the centrifugal instability emerges. This 3-D mode induces streamwise vortices and can become the most unstable mode. Rayleigh–Taylor instability can exist in a flow with acceleration when density gradients are present. It can be caused by a body force (e.g., gravity). In the situation when body force is absent, R-T instability could exist in a curved flow with density gradient. In our flow with negligible gravity force, the centrifugal force acts like "pseudo gravity" and could induce R-T instability. For the two-dimensional shear layers considered in this paper, the centrifugal and R-T instabilities could coexist. Although both the centrifugal and R-T instabilities could produce three-dimensional unstable structures, some of the important effects due to the centrifugal force are still present in the two-dimensional flows. The linear analysis performed by Liou [12] demonstrated that the centrifugal force could enhance or suppress the K-H mode in a two-dimensional curved shear layer with constant density. Zhuang [13] included the effects of density gradient in a curved shear layer and showed modifications of the K-H mode. We consider here only two-dimensional curved flows; the effects of three-dimensionality are left to future studies.

In reacting mixing layers, the stability characteristics could be different from those in nonreacting mixing layers, due to the modifications of the flow profiles caused by the chemical reactions. The effects of heat release on the instability of straight, reacting mixing layers were studied by Shin and Ferziger [14] by linear stability theory. An inviscid, low-Mach-number stability equation was derived and solved numerically. With a sufficient amount of heat release, multiple unstable modes (referred to as the outer modes), in addition to the central mode (the unstable mode associated with the central inflection point of the mean-velocity profile), were found. The outer modes arose due to the modifications of the density and velocity profiles caused by the chemical reactions, and were quite insensitive to the further increases in heat release. The central modes were suppressed significantly by the further increases in heat release so that the outer modes could become the dominant unstable modes. Shin and Ferziger [15] extended their previous work to include effects of high Mach numbers. Multiple supersonic unstable modes were found in both the nonreacting and reacting flows when the phase velocity of the disturbance was supersonic relative to the freestream. The supersonic modes became less unstable with increasing Mach number, but more unstable with increasing heat release. These modes did not enhance mixing of the two streams.

Two-dimensional straight (unidirectional) and curved mixing layers with imposed streamwise accelerations have been studied by Cheng et al. [16,17]. The streamwise acceleration showed stabilizing effects on both the nonreacting and reacting mixing layers, and could reduce the global chemical conversion rate. There, the streamwise acceleration was imposed by contracting and expanding the channel spanwise dimension, while keeping the channel transverse dimension constant. Here, the streamwise acceleration is imposed by contracting and expanding the channel transverse dimension, while keeping the channel spanwise dimension constant throughout. The flow converges and diverges accordingly, and the flowfield is modified significantly. We focus on the effects of the converging–diverging side walls on the instability and the combustion process. The discussions of the governing equations and numerical scheme are presented in Sec. II. The boundary conditions are given in Sec. III. The straight mixing layers in the converging–diverging channel are presented in Sec. IV, and the mixing layers in the curved converging–diverging channel and the turbinelike passage are investigated in Sec. V. The concluding remarks are given in Sec. VI.

II. Governing Equations and Numerical Method

The flow within a turbine-blade row is at high speed and often transonic. There are gradients of pressure, density, and velocity in the flowfield, in both the streamwise and transverse directions. Because the geometry of the turbine passage is rather complex, we simplify the physical problem to simulations of mixing layers passing through straight and curved channels in this paper. For this simplified geometry, the effects of the streamwise acceleration and transverse acceleration are retained. Because of the limitation of the 2-D numerical simulation, 3-D effects are omitted in this study. The effects of vortex stretching and the development of 3-D instabilities are neglected. Also, the small-scale turbulent structures are not resolved, due to the limitations in grid resolution.

The computational domains for the straight and curved converging–diverging channels are shown in Figs. 1a and 1b, respectively. The streamwise pressure gradient is imposed by contracting and expanding the transverse channel dimension in the x–y plane. The planar mixing layer enters the channel from the left. For the curved case, the air and fuel streams can be placed on either the inside or outside of the curve. The channels here are different from those studied previously by Cheng et al. [16,17] in which the streamwise pressure gradient was imposed by contracting and expanding the channel width in the spanwise direction, while keeping the channel transverse dimension constant.

The governing equations are the two-dimensional, compressible, multicomponent, Navier–Stokes equations with chemical source terms. There are a total of eight governing equations: the continuity
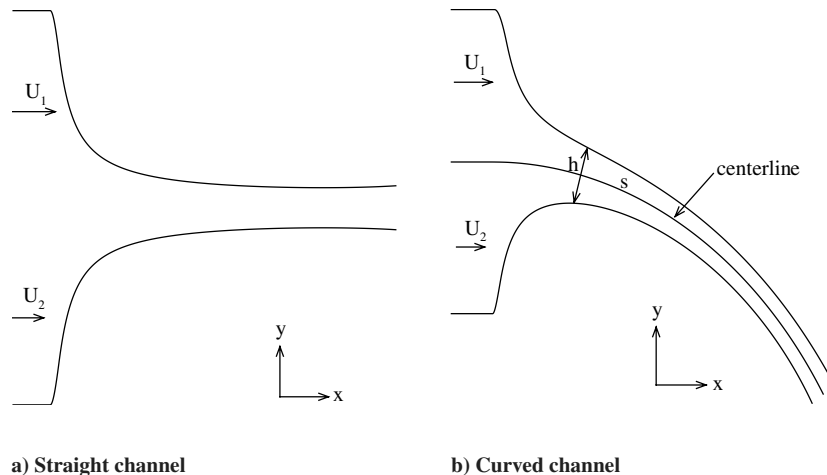

a) Straight channel   b) Curved channel

Fig. 1   Side view of the class II channels.

equation for the total density, the momentum equations in x and y directions, the energy equation, and the species continuity equations of O_2, CH_4, H_2O, and CO_2. Perfect gas is assumed. The equations written in conservation form are as follows:

$$\frac{\partial \mathbf{w}}{\partial t} + \frac{\partial \mathbf{f}}{\partial x} + \frac{\partial \mathbf{g}}{\partial y} - \frac{\partial \mathbf{f}_\mu}{\partial x} - \frac{\partial \mathbf{g}_\mu}{\partial y} = \mathbf{s} \tag{1}$$

where $\mathbf{w}$ is the vector of the conservative variables of mass, momentum, and energy, the vectors $\mathbf{f}$ and $\mathbf{g}$ are the inviscid fluxes, $\mathbf{f}_\mu$ and $\mathbf{g}_\mu$ are the viscous fluxes, and $\mathbf{s}$ is the source term. These terms are given as

$$\mathbf{w} = \begin{pmatrix} \rho \\ \rho u \\ \rho v \\ \rho E \\ \rho_n \end{pmatrix}, \quad \mathbf{s} = \begin{pmatrix} 0 \\ 0 \\ 0 \\ \dot{Q} \\ \dot{\omega}_n \end{pmatrix}, \quad \mathbf{f} = \begin{pmatrix} \rho u \\ \rho uu + p \\ \rho vu \\ \rho Hu \\ \rho_n u \end{pmatrix}, \quad \mathbf{g} = \begin{pmatrix} \rho v \\ \rho uv \\ \rho vv + p \\ \rho Hv \\ \rho_n v \end{pmatrix} \tag{2}$$

$$\mathbf{f}_\mu = \begin{pmatrix} 0 \\ \tau_{xx} \\ \tau_{yx} \\ u\tau_{xx} + v\tau_{yx} - q_x - \sum_{n=1}^N \rho_n u_{dn} h_n \\ -\rho_n u_{dn} \end{pmatrix} \tag{3}$$

$$\mathbf{g}_\mu = \begin{pmatrix} 0 \\ \tau_{xy} \\ \tau_{yy} \\ u\tau_{xy} + v\tau_{yy} - q_y - \sum_{n=1}^N \rho_n v_{dn} h_n \\ -\rho_n v_{dn} \end{pmatrix} \tag{4}$$

Time is represented as t; ρ_n is density for species n, where $n = 1, \ldots, 5$; p is pressure; μ is molecular viscosity; u and v are the flow velocity components in the x or y directions, respectively. Other quantities are

$$\tau_{ij} = 2\mu \left[\frac{1}{2} \left(\frac{\partial u_i}{\partial x_j} + \frac{\partial u_j}{\partial x_i} \right) - \frac{1}{3} \frac{\partial u_k}{\partial x_k} \delta_{ij} \right] \tag{5}$$

$$q_j = -C_p \frac{\mu}{Pr} \frac{\partial T}{\partial x_j} \tag{6}$$

$$h = \sum_{n=1}^N Y_n h_n, \quad \text{and} \quad h_n = \int_{T_0}^T C_{pn} \, dT \tag{7}$$

$$H = h + \frac{1}{2}(u^2 + v^2), \quad E = H - \frac{p}{\rho} \tag{8}$$

$$\dot{Q} = -\sum_{n=1}^N \dot{\omega}_n h_n^0 \tag{9}$$

$$\rho_n \mathbf{V}_{dn} = -\rho D_n \nabla \left(\frac{\rho_n}{\rho} \right) = -\rho D_n \nabla Y_n \tag{10}$$

where τ_{ij} is the viscous stress tensor with the standard tensor notation. The subscript indices i and j take either value x or y. The heat of formation of species n at the reference temperature T_0 is h_n^0, C_{pn} is the specific heat at constant pressure of species n, $\mathbf{V}_{dn} =$

(u_{dn}, v_{dn}) is the diffusion velocity of species n, and D_n is the diffusion coefficient. For a unity Schmidt number and Prandtl number, $D_n = \mu/\rho$ for all species. C_{pn} and h_n vary with temperature; they are given by NASA polynomials.

Methane (CH_4) is used for the current computations, although the method is not restricted to only one type of fuel. The combustion process is described by a one-step overall chemical reaction as follows:

$$CH_4 + 2O_2 + 7.52N_2 \rightarrow CO_2 + 2H_2O + 7.52N_2$$
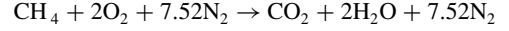
The chemical kinetics rate for the fuel is

$$\dot{\omega}_F = -W_F A e^{-E_a/RT} [\text{Fuel}]^a [O_2]^b \tag{11}$$

where the brackets [ ] represent molar concentration in mol/cm^3, and W_F is the molecular weight of fuel. For methane (CH_4), the parameter values [18] are $A = 2.8 \times 10^9$ $1/s$, $E_a = 48.4$ kcal/mol, $a = -0.3$, and $b = 1.3$.

The average gas constant R, molecular weight W, and viscosity coefficient μ can be obtained by the following equations:

$$R = \sum_{n=1}^N R_n Y_n, \quad \frac{1}{W} = \sum_{n=1}^N \frac{1}{W_n} Y_n, \quad \mu = \sum_{n=1}^N \mu_n(T) Y_n \tag{12}$$

The molecular viscosity coefficient of each species μ_n is obtained [19] by using the Sutherland law:

$$\frac{\mu_n}{\mu_{0n}} = \left(\frac{T}{T_0} \right)^{\frac{3}{2}} \frac{T_0 + 110}{T + 110} \tag{13}$$

where T_0 is the reference temperature (298.15 K), and μ_{0n} is the reference viscosity evaluated at T_0.

Before discretization, Eq. (1) in the physical domain is transformed to a generalized curvilinear coordinate system (ξ, η) by a transformation $\xi = \xi(x, y)$ and $\eta = \eta(x, y)$. The transformation is employed for the ease of treating curved walls and/or nonuniform meshes. The equations in (ξ, η) and the transformation metrics can be found in Cheng et al. [17].

A flux-splitting algorithm similar to that used by Steger and Warming [20] is used for spatial discretization of the inviscid flux. The inviscid flux is split into positive and negative parts according to the signs of the local eigenvalues of the flux Jacobian. A second-order upwind total-variation-diminishing scheme [21] using the van Leer limiter is employed. Second-order central differencing is used for the viscous flux, and a second-order Runge–Kutta multistage scheme is implemented for time marching. Because explicit time marching is used, the size of the time step is limited by the very small grid size at the center of the channel, rather than by the chemical source terms. The numerical scheme has been validated against flows with known analytic solutions and other computational fluid dynamics solutions, giving satisfactory results [16,17].

III. Boundary Conditions

There are four boundaries in the computational domain: inlet, exit, and upper and lower walls. Values of the conservative variable w and other physical properties must be known at the boundaries at each time step for the closure of the finite difference equations.

A. Inlet Conditions

At the inlet, the density, streamwise velocity, and mass fractions are specified as hyperbolic-tangent functions, and the cross stream velocity is set to zero. For example, u is specified as follows:

$$u(y) = \bar{U} \left[1 + \lambda \tanh \left(\frac{y}{2\delta_\theta} \right) \right] \tag{14}$$

where $\lambda \equiv (U_1 - U_2)/(U_1 + U_2)$, $\bar{U} \equiv (U_1 + U_2)/2$, and δ_θ is a reference value, which is a measure of the mixing-layer thickness at the inlet; δ_θ has a value of 0.000125 m in all cases. The density and

mass fractions of O_2 and CH_4 are specified in the same manner. The mass fraction of N_2 is equal to $1 - Y_{O_2} - Y_{CH_4}$. To reduce reflections of waves at the inlet, the local one-dimensional characteristic equations are solved [22,23] at the inlet for pressure. With this formulation, pressure waves coming from the interior can pass through the inlet plane. The temperature of the mixing layer is calculated from the perfect gas relation using the updated pressure. Because the fractional change in freestream pressure is very small, the freestream temperature remains approximately constant, and the temperature profile is similar to a hyperbolic-tangent distribution. Other nonspecified quantities can be calculated accordingly by thermodynamic relations.

B. Exit Conditions

For the cases without imposed streamwise pressure gradients, the Mach number at the exit is less than one; therefore, one physical condition at the exit plane must be specified to maintain uniqueness and well posedness. At the exit plane, the average value of pressure across the vertical or radial direction is specified. This allows a nonuniform distribution of pressure at the exit plane. To find the remaining variables and to allow passage of waves at the exit, we follow the common practice [24] and set the 1-D Lagrangian derivatives for ρ_i, ρu, and ρv to zero. For the cases with imposed streamwise pressure gradients, the flows achieve supersonic speed at the exit; therefore, extrapolation of variables from the interior is applied at the exit plane.

C. Side-Wall Conditions

Because our focus is on the mixing layer, the side walls are treated as inviscid and impermeable to save computational resources. Slip conditions are applied at the walls, the normal component of velocity is zero at the walls, and temperature gradient in the normal direction is set to zero.

IV. Mixing Layer in the Straight Channel

In previous work by Cheng et al. [17], the streamwise pressure gradient was imposed in a quasi-3-D manner by contracting and expanding the channel span (or channel width) in the z direction, while keeping the channel transverse dimension (or channel height) constant. This converging–diverging channel is described as the class I straight channel in [17]. The flow properties were uniform in the z direction and represented the average values across the channel span, and the deflections of the flow at the side walls were neglected. In this paper, the pressure effects of the side walls are accurately captured; the streamwise pressure gradient is imposed by contracting and expanding the channel dimension in the y direction of the x–y plane, as shown in Fig. 1a, and we refer this converging–diverging channel as the class II straight channel. For the class II straight channel, the streamlines converge and diverge in accordance with the varying channel transverse dimension. The effects of the contraction and expansion of the streamlines on the development of the mixing layer are investigated.

The height at the inlet of the class II straight channel is 0.06 m ($480\delta_\theta$), and the length of the channel l is 0.11 m ($880\delta_\theta$), where $\delta_\theta = 0.000125$ m. The inlet height and the channel length are the same as those for the class I straight channel. The contraction ratio of the class II channel height, however, is different from that for the class I straight channel. For the class I straight channel, the channel width in the z direction was designed to introduce a linearly

decreasing pressure distribution in the streamwise direction, and the pressure distribution caused the channel width to converge very sharply in the low-Mach-number regime. With the same linear pressure distribution, the class II straight channel would have very steep side walls that caused some numerical problems. Therefore, for the class II straight channel, the channel height is designed such that the pressure drops with $x^{1.5}$, so that the channel height initially converges relatively slowly. Based on the isentropic calculation, the total fractional pressure drop in the class II straight channel is kept the same as that in the class I straight channel, so that the average streamwise accelerations through the channels remain similar in the class I and class II straight cases. To evaluate the effects of the nonlinear pressure gradient, we have recomputed the reacting case in the class I straight channel with the nonlinear pressure gradient. The instability and the global chemical conversion rate are enhanced with the nonlinear pressure gradient; however, the differences are insignificant compared to the effects imposed by the converging–diverging side walls in the class II straight channel. For instance, the global chemical conversion rate for the reacting mixing layer in the class I straight channel with the nonlinear pressure gradient is approximately 20% higher than that for the reacting case in the class I straight channel with the linear pressure gradient. However, the global chemical conversion rate for the class II straight case is more than 6 times as high as that for the class I straight case. Because the effects of the geometry in the class II straight channel dominate the effects due to the discrepancy in the prescribed pressure gradients, it is not necessary to recalculate the class I cases [17], and they will be used as the base cases for comparison. The computational domain consists of 961 and 641 grid points in the streamwise and transverse directions, respectively. The grid sizes are slightly stretched in the streamwise direction and range from 9.6×10^{-5} m to 1.28×10^{-5} m. Because the height of the channel varies significantly in the streamwise direction, the grid spacings in the transverse direction $\triangle y$ at the centerline vary by an order of magnitude with downstream locations. At the centerline, $\triangle y$ is approximately 7.33×10^{-5} m at the inlet and 7.68×10^{-6} m near the throat of the nozzle.

Both nonreacting and reacting mixing layers are considered in the following sections. The inflow parameters are summarized in Table 1. The Reynolds numbers at the inlet Re_δ are calculated from ΔU, δ_θ, and the mean viscosity. For all cases, a Courant–Friedrichs–Lewy (CFL) number of 0.5 is used, and virtually identical results are obtained with smaller CFL numbers.

A. Nonreacting Mixing Layer in the Straight Channel

Numerical simulations for the nonreacting mixing layer passing through the class II straight channel have been performed. The mixing layer is composed of a hot airstream and a cold fuel stream of different streamwise velocities. The boundary conditions are specified in Sec. III. In this section, all the instantaneous flowfields for the class II straight cases are shown at 7.9 residence time unless otherwise stated. The residence time is calculated based on the channel length and the average streamwise velocity of the two streams.

Because of the imposed streamwise favorable pressure gradient, the channel is choked, and the mixing layer accelerates from low subsonic speed at the inlet to low supersonic speed at the exit. The time-averaged Mach numbers of the two streams are ≈ 0.06 at the inlet and ≈ 1.31 at the exit. The instantaneous streamwise velocity and Mach number profiles in the supersonic regime ($x = 816\delta_\theta$) are

Table 1   Summary of inflow conditions for class II straight channel (units of velocity, temperature, and density are m/s, K, and kg/m^3, respectively)

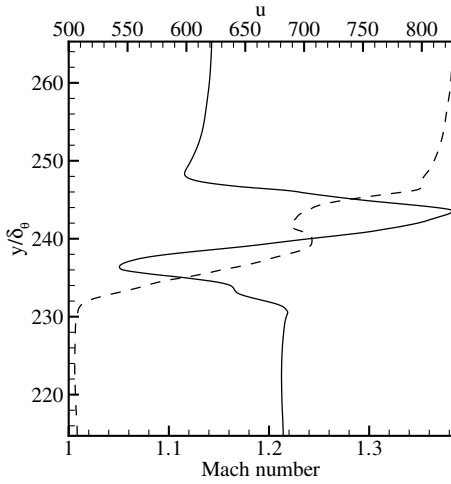|	Acceleration	Reaction	u_1[a]	u_2[b]	T_1[a]	T_2[b]	ρ_1[a]	ρ_2[b]	Re_δ
Case 1	Yes	No	50	25	1650	300	2.19	6.67	415
Case 2	Yes	Yes	44.7	22.3	1650	300	2.45	7.51	372

[a]Air
[b]Fuel

Fig. 2 Instantaneous streamwise velocity (m/s) and Mach number profiles at $x = 816\delta_\theta$ for the nonreacting case [solid line, Mach number (lower horizontal axis); dashed line, streamwise velocity (upper horizontal axis)].

shown in Fig. 2. Both the streamwise velocity and Mach number profiles show local maxima and minima across the transverse direction. The unsteady vortical motions in the mixing region can induce local accelerations and decelerations and are the major cause for the nonmonotonic streamwise velocity profile. The hot air and cold fuel are entrained to the vortical structures; because of the "swirls," the species mass fractions also exhibit local maxima and minima. The local speed of sound, which strongly varies with the chemical composition and temperature of the mixture, becomes nonmonotonic across the mixing layer. Consequently, the Mach number profiles exhibit local peaks across the transverse direction. The streamwise pressure gradient in the class II straight channel is different from that in the class I straight channel, and hence the streamwise accelerations are slightly different in the two cases. The time-averaged pressure distributions along the centerlines of the channels are shown in Fig. 3. For the class I straight channel, the pressure decreases linearly after passing a short constant-pressure section. The pressure in the class II straight channel decreases smoothly and relatively slowly. Although there are substantial differences in the values of pressure, the pressure gradients are still comparable. Computational results show that the differences are relatively insignificant.

Because of the curvature of the side walls, the flowfield in the class II straight channel differs from that in the class I straight channel and exhibits several new phenomena. Because the channel is

contracting and expanding in the x–y plane, the streamlines converge and diverge accordingly. When the channel starts to curve, the streamlines at the walls turn sharply. Because slip conditions are applied at the walls, no flow separation occurs. In the converging portion of the channel, significant transverse velocity comparable to the local streamwise velocity is induced. The mixing of the two fluids and the thickness of the mixing layer can be observed from instantaneous contours of temperature (not shown here for brevity). It is observed that the thickness of the mixing layer (based on the temperature field) decreases with increasing downstream distance in the converging portion of the channel. The thickness of the mixing layer appears to stay relatively constant in the region passing $x \cong 300\delta_\theta$ and before roll up occurs. In that region, the channel height varies slightly with downstream locations. The development of the mixing layer is further investigated by measuring the growth of the mixing-layer thickness. The mixing-layer thickness is determined from the time-averaged streamwise velocity profile, and the measurements are taken at various x locations between 80 and $230\delta_\theta$. This region covers the sharply converging portion of the channel with the significant effects of the converging streamlines. Figure 4 shows the thickness δ_u of the mixing layer normalized by the value at $x = 80\delta_\theta$ (δ_{u0}). The thickness of the mixing layer is defined by the points where the local streamwise velocity reaches 99% of its freestream value. For the class I straight channel, the streamwise acceleration inhibits the growth of the mixing layer so that the thickness increases slowly. For the class II straight channel with its smaller pressure drop, the streamwise acceleration in the considered region is not as great as that in the class I straight channel (see Fig. 3). The streamwise acceleration suppresses the growth of the mixing layer, and the thickness decreases through the region because the flow is converging.

Because the thickness of the mixing layer becomes thinner in the class II straight channel, the gradients of the flow variables in the transverse direction may become larger. In general, downstream of the sharply converging section, the magnitude of the peak vorticity is larger for the class II straight channel than that for the class I straight channel. For instance, the instantaneous vorticity profiles at $x = 270\delta_\theta$ for the class I straight channel and the class II straight channel are shown in Fig. 5. The dominant vorticity is in the clockwise direction (negative vorticity); the magnitude of the peak vorticity for the class II straight channel is approximately 50% larger than that for the class I straight channel at that location. The increase in magnitude of the peak vorticity for the class II straight channel is contributed mainly by the enhanced baroclinic effect. The vorticity dynamics are examined in the equation shown here:

$$\frac{D\omega_z}{Dt} = \frac{1}{\rho^2} \nabla\rho \times \nabla p - \omega_z \nabla \cdot \mathbf{u} + \text{viscous term} \qquad (15)$$
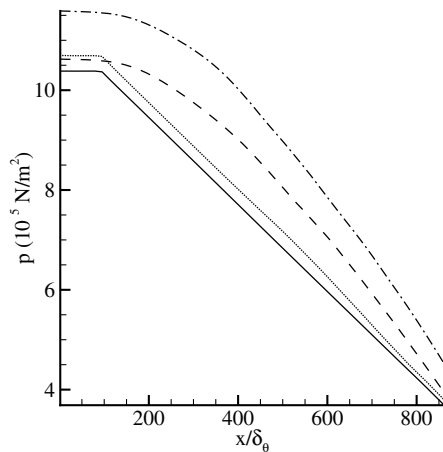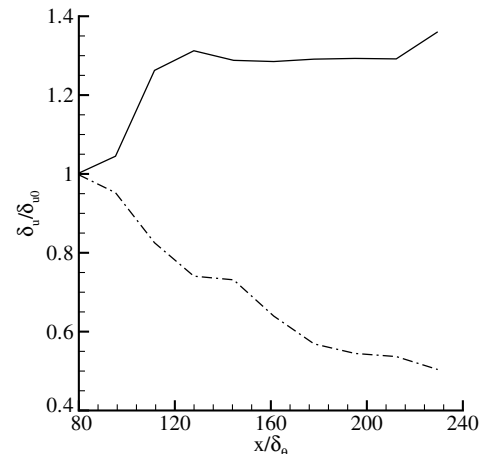

Fig. 3 Time-averaged pressure distribution at the centerline along the channel (solid line, class I straight channel, nonreacting; dashed line, class II straight channel, nonreacting; dotted line, class I straight channel, reacting; dashed-dotted line, class II straight channel, reacting).

Fig. 4 Ratio of mixing-layer thickness (solid line, class I straight channel; dashed-dotted line, class II straight channel).
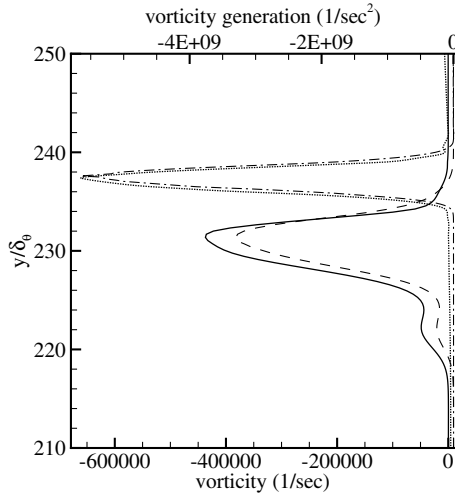
Fig. 5 Instantaneous vorticity profile and vorticity generation by the baroclinic effect at $x = 270\delta_\theta$ for the nonreacting straight cases (solid line, vorticity for the class I channel; dotted line, vorticity for the class II channel; dashed line, baroclinic effect for the class I channel; dashed-dotted line, baroclinic effect for the class II channel).
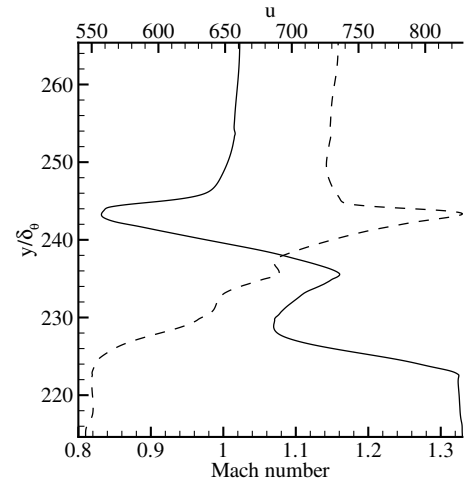

Fig. 6 Instantaneous streamwise velocity (m/s) and Mach number profiles at $x = 824\delta_\theta$ for the reacting case [solid line, Mach number (lower horizontal axis); dashed line, streamwise velocity (upper horizontal axis)].

Because the flow is two-dimensional, the term associated with the deformation of vortex lines vanishes. The viscous term is, in general, 1 order of magnitude smaller than the other terms; therefore, we only focus on the production of vorticity associated with the baroclinic effects and the divergence of the velocity field. The baroclinic term defined in Eq. (15) intensifies the vorticity and is more significant than the divergence term that weakens the vorticity. Figure 5 shows that the vorticity generation by the baroclinic effect for the class II straight channel is enhanced substantially; the enhanced baroclinic term is due to the increased density gradient in the transverse direction. Because the peak vorticity is more intense in the class II straight channel, we expect that the instability of the mixing layer is also enhanced. The instability will be discussed in the next section.

B.   Reacting Mixing Layer in the Straight Channel

The mixing layer with chemical reactions passing through the class II straight channel is investigated in this section. The geometry of the channel and the grid are identical to those for the nonreacting case considered in the previous section; however, the inflow and boundary conditions have been modified for the reacting mixing layer. For the boundary conditions implemented for the previous nonreacting case, the density was held constant and the temperature was calculated from the perfect gas relation with pressure determined from the local 1-D characteristic equation. For the reacting mixing layer, the pressure at the inlet increases due to the modified choked condition associated with the chemical reactions, and the temperature at the inlet rises accordingly. To hold the temperature profile constant at the inlet, we now specify the temperature and mass fractions for the species as hyperbolic-tangent functions similar to Eq. (14). The pressure is again calculated from the local 1-D characteristic equation. The total mass flow rate is held constant and is the same as that for the corresponding nonreacting case. The density is obtained from the perfect gas relation, and the streamwise velocity can be determined from the density and the constant mass flow rate. For these inflow conditions, the velocity shear at the inlet is not constant, but the product of ρu remains the same as that in the corresponding nonreacting case. In this section, all the instantaneous flowfields for the class II straight channel are shown at 5.9 residence time unless otherwise stated. The reacting mixing layer is again choked and accelerates from low subsonic speed at the inlet to low supersonic speed at the exit; the time-averaged Mach numbers of the two streams are approximately 0.054 at the inlet and 1.27 at the exit. The instantaneous streamwise velocity and Mach number profiles in the supersonic regime ($x = 824\delta_\theta$) are shown in Fig. 6. The large velocity peak in the figure corresponds to the combustion region in

which the temperature is very high. Because the density in the combustion region is substantially lower than that in the surrounding fluid, the imposed streamwise pressure gradient causes large acceleration, which results in the large local streamwise velocity peak. This phenomena was also observed in the class I straight and curved reacting mixing layers [16,17]. Because the local speed of sound is high in the hot region, the Mach number drops in the combustion region even though the velocity attains its local maximum. The local peak in the Mach number profile in the nonreacting region is caused by the unsteady vortical motions discussed in Sec. IV.A. The time-averaged pressure distribution for the reacting case is compared with the nonreacting cases in Fig. 3. The pressure for the reacting mixing layer at the inlet plane rises, and the density increases accordingly because temperature is constant. As a consequence, the streamwise velocity has to decrease to maintain the specified constant mass flow rate, resulting in the lower Mach numbers for the inflows. Farther downstream, the rate of pressure drop is comparable with the other nonreacting cases.

Similar to the nonreacting case, the mixing-layer thickness decreases as the flow passes through the converging portion of the channel, and the transverse gradients of flow properties may become larger compared with the corresponding class I straight case. As an example, the instantaneous vorticities for the class II straight channel and the class I straight channel are shown in Fig. 7. The streamwise locations for both profiles correspond to $x = 280\delta_\theta$. At that location, the mixing-layer thickness for the class II straight case has decreased
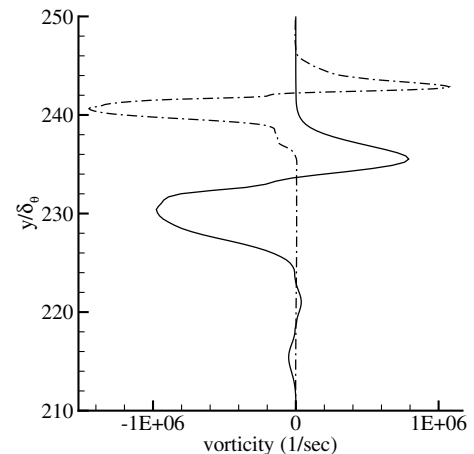

Fig. 7 Instantaneous vorticity profiles at $x = 280\delta_\theta$ for the reacting mixing layers (solid line, class I straight channel; dashed-dotted line, class II straight channel).

substantially relative to its initial value at the inlet and is smaller than that for the class I straight case. Therefore, both the negative and positive vorticities become more concentrated in the class II straight channel and have larger peak magnitudes than those in the class I straight channel. The counter-rotating vortices are generated by the local streamwise velocity peak. Positive vorticity is generated above the velocity peak, and negative vorticity is generated underneath. Because of the larger velocity gradient below the velocity peak, the negative vorticity is more intense than the positive one.

The instantaneous temperature contours indicate that both the nonreacting and reacting mixing layers in the class II straight channel are much more unstable than the corresponding cases in the class I straight channel. This observation is consistent with the instability measured by the integrated turbulent kinetic energy flux defined as follows:

$$KE(s) = \int_0^h [\overline{\rho u_s (u_s^2 + u_r^2)} - \overline{\rho u_s}(\bar{u}_s^2 + \bar{u}_r^2)] \, dy \qquad (16)$$

where s is the streamwise location along the centerline, $\bar{(\ )}$ indicates a time-averaged property, and u_s and u_r are the streamwise and transverse components of velocity, respectively; the integration is carried out from the lower wall to the upper wall along the transverse direction. Although not shown here, the computed magnitude of the turbulent kinetic energy for the class II straight case is several times larger than that for the corresponding class I straight case. Because the effects associated with the converging–diverging side walls are absent in the class I straight channel, we deduce that the destabilizing effect in the class II straight channel is contributed by the modified flow profiles caused by the converging–diverging side walls; in particular, the more concentrated vorticity in the class II case is likely to enhance instability. For the class II straight channel, the reacting case is more unstable than the corresponding nonreacting one. For the reacting mixing layer, there are multiple inflection points in the streamwise velocity and density profiles associated with the local maxima and minima. On the other hand, only one inflection point exists in the streamwise velocity profile for the nonreacting mixing layer. Therefore, the modified streamwise velocity profile due to the chemical reaction can alter the instability mechanism significantly and contributes to the enhanced instability.

The converging–diverging side walls in the class II straight channel impose profound effects on the development of the flame structures and the chemical conversion rate. The instantaneous contours of temperature are shown in Fig. 8. The flame is defined as the location at which a local maximum temperature in the transverse direction exists. In the figure, the flame region is illustrated by the darkened area between the air and fuel streams. It is observed that the flame region becomes thinner with increasing downstream distance in the sharply converging portion of the channel, and this finding is
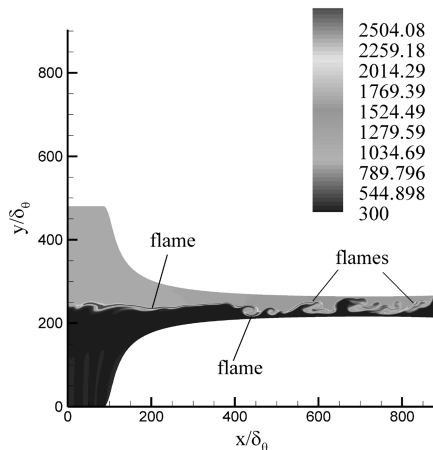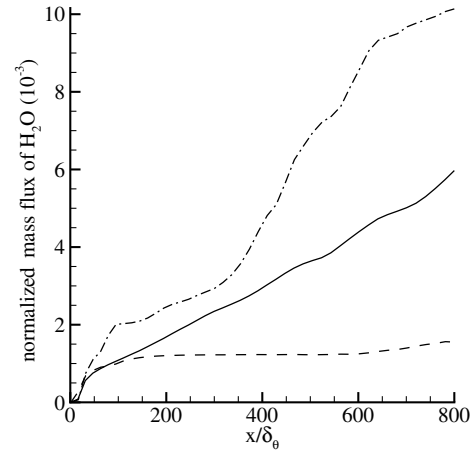

Fig. 9   Time-averaged mass flux of H$_2$O normalized by the total mass flux (solid line, straight channel, nonaccelerating; dashed line, class I straight channel; dashed-dotted line, class II straight channel).

consistent with the decreasing mixing-layer thickness found previously. Because of the instability, waviness develops as the flame region propagates, and the flame region tears into isolated segments further downstream. Flame tearing (local extinction) was also observed in the class I straight channel, but it occurred further downstream. Typically, flame tearing first occurs in between $x = 400$ and $500\delta_\theta$ in the class II straight channel, and beyond $x = 640\delta_\theta$ in the class I straight channel. In the class II straight channel, the unsteady flame regions are widely spread across the transverse direction and could appear near both side walls. This phenomenon was not observed in the corresponding class I straight channel. To investigate the efficiency of the chemical conversion process in the class II straight channel, the global conversion rates of H$_2$O for the straight reacting cases are compared in Fig. 9. The global conversion rate of H$_2$O is defined as the ratio of the mass flow rate of H$_2$O over the total mass flow rate as follows:

$$\dot{m}_{\mathrm{H_2O}} = \frac{\int_0^h \bar{\rho}_{\mathrm{H_2O}} \bar{u} \, dy}{\int_0^h \bar{\rho} \, \bar{u} \, dy} \qquad (17)$$

where $\bar{(\ )}$ represents a time-averaged quantity, and the integrals are evaluated at fixed streamwise locations along the centerline. Because the products of H$_2$O and CO$_2$ are formed, diffused, and advected in stoichiometric proportions, the mass flux calculation in Eq. (17) indicates the amount of product that has been created in the flow up to a specified streamwise position. The global chemical conversion rate is much enhanced in the class II straight channel and is approximately 6.4 times larger than that in the class I straight channel near the exit plane. For a better understanding of the global chemical conversion rate, we have examined the local heat release rates (essentially chemical reaction rates) and their distributions in the flowfields at different times. For the class II straight case, regions of high heat release rates are often found in the mixing regions near the inlet and in the downstream regions where large unstable structures are formed. These regions are formed periodically in the downstream portion beyond $x = 400\delta_\theta$ in the class II straight channel and traverse the channel cross section. High heat release rates in the class I channel are found in small regions near the inlet and found sparsely in the unstable structures near the centerline beyond $x = 640\delta_\theta$. The distribution of the local heat release rate indicates that chemical reaction is enhanced in regions with unstable vortical development. The mixing of the fluids is significantly enhanced in the class II straight channel associated with the development of the unstable structures, so that the chemical reaction rate is enhanced. Note that the global chemical conversion rate for the class II straight case is also larger than that for the corresponding nonaccelerating straight case. This result is also due to the relatively better mixing of fluids in the class II straight channel.

Fig. 8   Instantaneous contours of temperature (Kelvin) for the reacting mixing layer in the class II straight channel.

V. Mixing Layer in the Curved Channel

The curved mixing layer subjected to both imposed streamwise and transverse accelerations is studied in this section. Two types of curved channel are considered. For the first type, the channel shape is designed from a prescribed pressure gradient and is similar to the constant-span straight channel. For the second type, the channel shape is modified from the two-dimensional plane of an actual turbine passage. The major features of the mixing layer in the turbinelike passage are identified and compared with those in the constant-span curved channel.

A. Mixing Layer in the Constant-Span Curved Channel

The curved mixing layer subjected to both imposed streamwise and transverse accelerations is studied in this section. Similar to the class II straight channel in Section IV, the streamwise pressure gradient is imposed by contracting and expanding the channel height in the x–y plane. This constant-span curved converging–diverging channel is named the class II curved channel; the curved converging–diverging channel in the previous work by Cheng et al. [17] is named the class I curved channel. For the class II curved channel, the channel height contracts and expands in the x–y plane with downstream distance, and the mixing layer converges and diverges accordingly. This phenomenon was absent in the class I curved channel, in which the streamwise acceleration was imposed by varying the channel width in the z direction and the channel height remained constant in the x–y plane.

The computational domain of the class II curved channel is shown in Fig. 1b. The channel starts with a small straight section (0.01 m) before it starts to curve. The height at the inlet of the nozzle is 0.06 m ($480\delta_\theta$), which is the same as that for the class I curved channel. The geometry of the centerline is also the same as that for the class I curved channel. The total length of the centerline is 0.11 m ($880\delta_\theta$), and s represents the distance measured along the centerline. The total turning angle is 1 rad. The height h of the nozzle is indicated in Fig. 1b. It is defined as the height of the local cross section normal to the centerline and varies with downstream distance. The variation of channel height along the centerline in the class II curved channel is identical to that in the class II straight channel. The computational domain consists of 961 and 641 grid points in the streamwise and transverse directions, respectively. A similar body-fitted curvilinear grid to that in the class II straight channel is used.

Both curved nonreacting and reacting mixing layers, each with two flow configurations, are considered in this section. The first flow configuration has a faster and hotter airstream on the outside of the curve, with a slower and colder fuel stream on the inside of the curve. The second configuration has the faster and hotter airstream on the inside of the curve, while the slower and colder fuel stream is placed on the outside of the curve. The first flow configuration is identified as either NFL-A-II or RFL-A-II, where the first letter designates nonreacting or reacting, the second letter designates faster or slower fluid on the outside of the curve, the third one designates lighter or heavier fluid on the outside of the curve, and the fourth letter designates imposed streamwise acceleration. Similarly, the second flow configuration is identified as either NSH-A-II or RSH-A-II. The suffix "II" distinguishes the cases in the class II curved channel from the class I curved cases. The inflow parameters and the boundary conditions are identical to those discussed in Sec. IV.B. The inflow conditions for the four curved cases are summarized in Table 2. The flow parameters in the table represent the time-averaged values in the freestreams over one residence time. Note that temperature, species
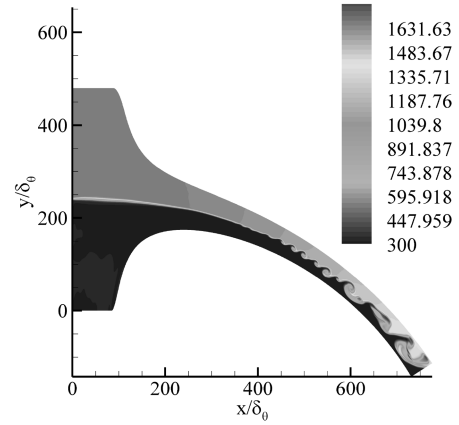

Fig. 10 Instantaneous contours of temperature (Kelvin) for the NFL-A-II case in the class II curved channel.

mass fractions, and total mass flow rate are held constant at the inlet, whereas other variables are allowed to vary with time. For all cases, a CFL number of 0.5 ensures numerical stability, and virtually identical results are obtained with smaller CFL numbers.

1. Nonreacting Mixing Layer in the Constant-Span Curved Channel

Nonreacting mixing layers passing through the class II curved channel are investigated in this section. The instantaneous flowfields for the NSH-A-II and NFL-A-II cases presented in this section are evaluated at residence times of 6.5 and 6.3, respectively. The statistical data have been gathered for a period of about 1.5 residence time for both cases, and the results are approximately time independent. The residence time is calculated based on the length of the centerline and the average streamwise velocity (tangent to the centerline) of the two streams. For both the NSH-A-II and NFL-A-II cases, the mixing layers accelerate from low subsonic speed at the inlet to low supersonic speed at the exit. For the NSH-A-II case, the time-averaged freestream Mach numbers at the exit are approximately 1.24 and 1.35 on the outside and inside of the curve, respectively. For the NFL-A-II case, the time-averaged freestream Mach numbers at the exit are approximately 1.24 and 1.32 on the outside and inside of the curve, respectively.

Similar to the class II straight cases in Sec. IV.A, the sharply converging side walls impose significant effects on the development of the mixing layer, and those effects are absent for the cases in the class I curved channel. In general, the mixing-layer thickness decreases in the sharply converging section of the channel, and the local peak vorticity becomes more concentrated. Also, the flow appears to be more unstable than the corresponding flow in the class I curved channel, and the unstable structures can occupy a large portion of the channel height. To illustrate the development of the mixing layer, the instantaneous contours of temperature for the NFL-A-II case are shown in Fig. 10; the flowfields for the NSH-A-II case, with the dominant vorticity in the counterclockwise direction (clockwise in the NFL-A-II case), are similar to those for the NFL-A-II case. In the figure, the dark scale represents the cold fuel, and the thin layer with light gray scale near the centerline represents the mixture of hot air and cold fuel. Based on observations, the class II curved cases are more unstable than the corresponding class I curved cases. For the class I cases, the mixing layers appeared laminar until near the exit of the channel where waviness developed, but roll up of

Table 2 Summary of the inflow conditions for the constant-span curved converging–diverging channel (units of velocity, density, and temperature are m/s, kg/m³, and K, respectively)

	Reaction	Vel. outside	Vel. inside	T outside	T inside	ρ outside	ρ inside	Re_δ
NSH-A-II	No	24.7	49.5	300	1650	6.76	2.22	412
NFL-A-II	No	49.3	24.7	1650	300	2.22	6.79	408
RSH-A-II	Yes	22.8	45.5	300	1650	7.35	2.42	377
RFL-A-II	Yes	43.4	21.7	1650	300	2.52	7.74	360

the mixing layer might or might not occur. For the class II nonreacting cases, the mixing layers start to roll up around $s = 400\delta_\theta$, which is approximately halfway downstream from the inlet. The unstable structures grow further downstream and can occupy a large proportion of the local cross section. Because the unstable structures come close to the side walls at some downstream locations, the cold fuel can be entrained to the freestream of the air side, or the hot air can be entrained to the freestream of the fuel side. More details of this phenomenon will be given in the discussion of the reacting cases.

Examination of the turbulent kinetic energies for the class II curved cases indicates that the class II curved cases NFL-A-II and NSH-A-II are several times more unstable than the corresponding class I curved cases. This result agrees with the observations discussed previously and again indicates that the constant-span converging–diverging channel imposes destabilizing effects on the mixing layers. The turning of the channel imposes mixed effects on the instability of the mixing layer; the centrifugal effect associated with the velocity profile and the R-T mechanism are competing against each other for both cases. The centrifugal instability associated with the velocity profile can be isolated from the R-T instability in a constant-density curved mixing layer. The numerical simulations [17] for such mixing layer showed that there was a destabilizing effect for the case with faster fluid on the inside but a stabilizing effect for the case with faster fluid on the outside. Therefore, it is expected that the streamwise velocity profile imposes a destabilizing effect for the NSH-A-II case and a stabilizing effect for the NFL-A-II case. On the other hand, the R-T mechanism should impose a stabilizing effect for the NSH-A-II case (heavier fluid on the outside) but a destabilizing effect for the NFL-A-II case (lighter fluid on the outside). The NFL-A-II case is more unstable than the NSH-A-II case, and this trend is consistent with that found in the class I curved channel. The instabilities of the class II straight case and the NSH-A-II case are very close to each other at most locations, and the straight case becomes slightly more unstable than the NSH-A-II case near the exit. This implies that, in the NSH-A-II case, the destabilizing and stabilizing mechanisms associated with the turning nearly balance each other, and the net effect by the velocity profile and the R-T mechanism may be sensitive to flow conditions and vary from one case to another.

2. Reacting Mixing Layer in the Constant-Span Curved Channel

Reacting mixing layers passing through the class II curved channel are investigated in this section. The instantaneous flowfields for the RSH-A-II and RFL-A-II cases are evaluated at residence times of 6.1 and 5.8, respectively. The statistical data have been gathered for a period of about 1.5 residence time for both cases, and the results are approximately time independent. Both the RSH-A-II and RFL-A-II cases are choked, and the mixing layers accelerate from low subsonic speed at the inlet to low supersonic speed at the exit. For case RSH-A-II, the time-averaged freestream Mach numbers at the exit are approximately 1.23 and 1.35 on the outside and inside of the curve, respectively. For case RFL-A-II, the time-averaged freestream Mach numbers at the exit are approximately 1.24 and 1.31 on the outside and inside of the curve, respectively.

The effects of the sharply converging side walls found in the previous sections are also present in the class II curved reacting cases. Because of the converging side walls, the thickness of the mixing layer decreases as the flow passes through the sharply converging section of the channel, and the peak vorticities (both positive and negative) become more concentrated than those in the class I curved cases. The instantaneous contours of vorticity for the RSH-A-II and RFL-A-II cases are shown in Figs. 11 and 12, respectively. To have better visualization of the vortex structures, the figures have been enlarged and only part of the channel is shown. For both cases, the positive-vorticity layer lies on top of the negative-vorticity layer as indicated in the figures. The counter-rotating vortices are caused by the streamwise acceleration and chemical reaction as discussed previously. For both cases, the magnitudes of the vorticities become larger with increasing downstream distance because of the
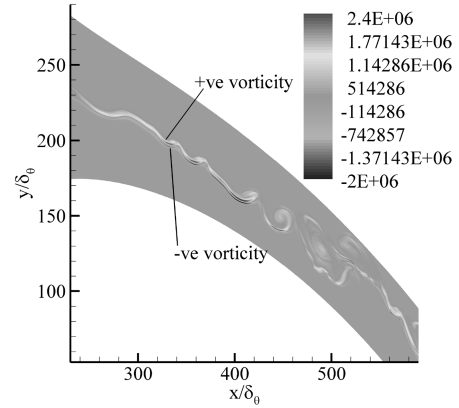

Fig. 11 Instantaneous contours of vorticity (1/s) for the RSH-A-II case in the class II curved channel.
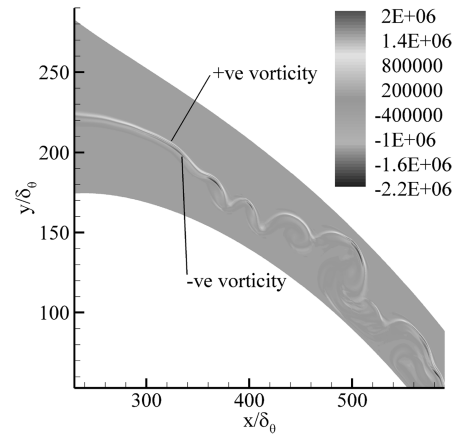

Fig. 12 Instantaneous contours of vorticity (1/s) for the RFL-A-II case in the class II curved channel.

streamwise acceleration. Roll ups of the vorticity layers are observed, and the vortices can appear near the side walls; for instance, a pair of counter-rotating vortices is found near the upper side wall at $x = 500\delta_\theta$ in Fig. 12. The RFL-A-II and RSH-A-II cases are much more unstable than their class I counterparts. The computed magnitudes of the turbulent kinetic energy for the class II curved cases are several times as large as those for the class I curved cases. These results indicate that there is a destabilizing effect imposed by the converging–diverging side walls in the class II curved channel, and this destabilizing effect was also found in the class II straight cases, as well as the class II curved nonreacting cases. Generalizing the findings in all the class II (straight and curved) cases, the enhanced instability relative to the class I cases is very likely linked to the reduction in the mixing-layer thickness, which results in more concentrated vorticity. The effect of the reduction in the mixing-layer thickness can also be deduced from the linear stability theory [16,25,26]. A two-dimensional disturbance can be modeled as a traveling wave as follows:

$$u'(x, y, t) = \hat{u}(y)e^{i(\alpha x - \omega t)} \tag{18}$$

where α is the wave number which is a complex number, and ω is the angular frequency. From the linear stability analysis for the nonreacting mixing layer with finite thickness, $\alpha_i \sim \lambda/\delta_\theta$ at a given frequency, where α_i is the imaginary part of α and represents the spatial growth rate; $\lambda = (U_1 - U_2)/(U_1 + U_2)$ represents the amount of "shear." For constant λ, α_i increases with decreasing δ_θ; therefore, the growth rate of the disturbance becomes larger, and the flow becomes more unstable within the same channel length. We find that the class II curved reacting cases are more unstable than the corresponding nonreacting cases. This finding is consistent with the

previous conclusion deduced from Sec. IV.B that the chemical reaction always destabilizes the mixing layer. The enhanced instability for the class II curved case is also caused by the modified flow profiles due to the chemical reactions. For instance, both the RFL-A-II and RSH-A-II cases exhibit local maxima in the streamline velocity profiles and local minima in the density profiles, and hence the instability mechanism is modified. For the class II curved channel, the RFL-A-II case is more unstable than the RSH-A-II case, and the instability of the straight case is in between the two curved cases. This trend is similar to that observed in the class I curved cases. For the RFL-A-II and RSH-A-II cases, the local minimum in density and the local streamwise velocity peak introduce competing effects (also observed in the class I curved cases) associated with the turning; the velocity profile and the density profile can individually impose a stabilizing effect on one side of the peak but a destabilizing effect on the other side. For example, based on the R-T mechanism, there is a destabilizing effect below the density trough but a stabilizing effect above the density trough. Also, the centrifugal effect associated with the velocity profile destabilizes the flow above the streamwise velocity peak but stabilizes the flow below the peak. Similar to the class I curved cases, multiple velocity and density peaks can exist across the turning mixing layers, and the instability mechanisms become even more complicated. The combined effects of the stabilizing and destabilizing mechanisms are determined by our numerical simulations. However, the relative importance of each is difficult to identify from the computational results.

Figures 13 and 14 show the instantaneous contours of temperature for the RFL-A-II and RSH-A-II cases, respectively. The flame region is illustrated by the darkened area between the air and fuel streams. For both cases, the flames appear more wavy and unstable than those in the class I c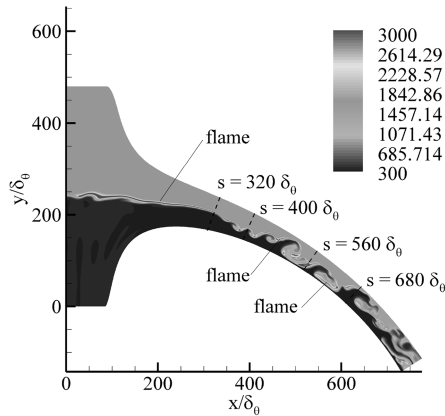urved channel, and the flame regions tear into isolated segments as the instability grows with increasing downstream distance. Relative to the class I curved cases, roll ups of the flame regions occur further upstream for the RFL-A-II and RSH-A-II cases. For both cases, roll ups typically occur between $s = 320$ and $400\delta_\theta$. The exact roll-up location in each case is difficult to determine, because the flow is not exactly periodic in time. Another important finding in the flame structure is that the flame region can appear very close to the side wall. For instance, for the RFL-A-II case, two flame locations near the side walls are identified at $s = 560$ and $680\delta_\theta$. At those locations, the majority of the channel cross section is occupied by either hot air or cold fuel. To illustrate this effect more clearly, the chemical compositions across the transverse direction at those locations are shown in Fig. 15. At $s = 560\delta_\theta$, the flame region is near the lower side wall. Slightly over 10% of the cross section is dominated by fuel, and the rest of the channel is occupied mostly by air and products. At $s = 680\delta_\theta$, the opposite result is observed. The flame region is near the upper side wall. Approximately 80% of the channel height is occupied by fuel, and the rest is occupied by air and products. Similar phenomenon also occurs in the RSH-A-II case, but it never happened in the class I curved channel. For the class I curved cases, the unstable structures primarily stayed in the vicinity of the centerline, and the chemical reactions did not occur near the side walls.

The global chemical conversion rates for the accelerating cases are compared in Fig. 16. The chemical conversion efficiency is greatly enhanced in the class II curved cases; this result is consistent with the finding from the class II straight cases. The global conversion rates for the class II curved cases are approximately 5.5–8 times as large as those for the corresponding class I curved cases. The mechanism by which the combustion process is enhanced is similar to that discussed in Sec. IV.B. In short, mixing of fluids is greatly enhanced in the class II curved channel due to the increased instability, so that the chemical reaction rate is enhanced. Also, high chemical reaction rates are frequently found in the mixing regions dominated by unstable vortical structures. Among the three cases in the class II curved channel, the RFL-A-II case is the one with the largest species conversion rate, the RSH-A-II case is the one with the least, and the straight case is in between the curved cases. This trend is similar to what we have observed in the class I accelerating and reacting cases, however, the differences in the global chemical conversion rates among the class II curved cases are more significant.

B.   Mixing Layer in the Turbinelike Passage

Two-dimensional simulations of nonreacting and reacting mixing layers passing through a turbinelike passage have been performed. The geometry is modified from a 2-D blade-to-blade passage of an

Fig. 13   Instantaneous contours of temperature (Kelvin) for the RFL-A-II case in the class II curved channel.

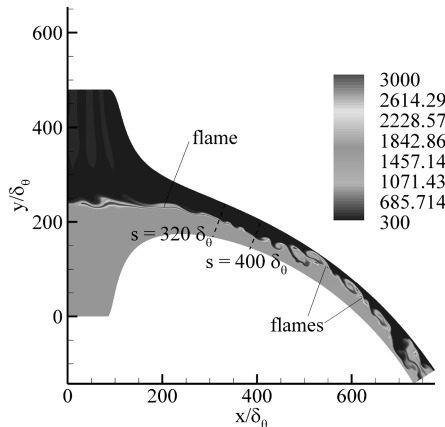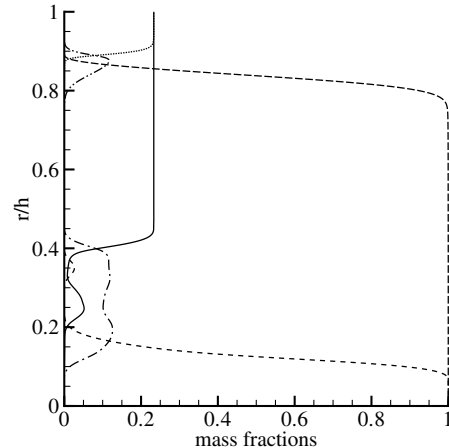**Fig. 14   Instantaneous contours of temperature (Kelvin) for the RSH-A-II case in the class II curved channel.**

Fig. 15   Instantaneous mass fractions in the transverse direction for the RFL-A-II case; r is the distance measured from the lower wall along the local cross section. At $s = 560\delta_\theta$, O_2 is the solid line, CH_4 is the dashed line, and H_2O is the dashed-dotted line. At $s = 680\delta_\theta$, O_2 is the dotted line, CH_4 is the long-dashed line, and H_2O is the dashed-double-dotted line.
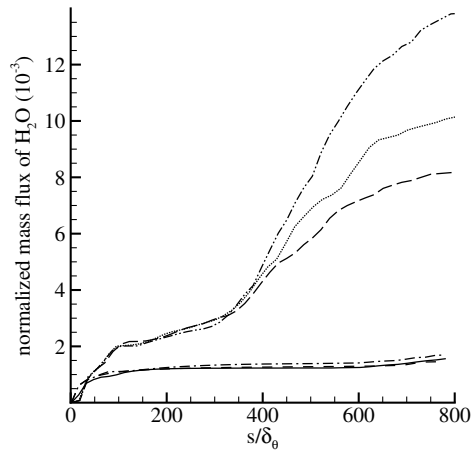
Fig. 16 Time-averaged mass flux of H_2O normalized by the total mass flux [class I straight case (solid line), case RSH-A (dashed line), case RFL-A (dashed-dotted line), class II straight case (dotted line), case RSH-A-II (long-dashed line), case RFL-A-II (dashed-double-dotted line)].

a) NFL-A-T case   b) RFL-A-T case

Fig. 17 Instantaneous contours of temperature (Kelvin) in the turbinelike passage.

actual turbine design. The computational domain includes the incoming stream through a gap upstream of the passage, the passage itself between the stator vanes, and a downstream gap between the stator and the rotor. The computational domain is discretized by 961 and 641 grid points in the x and y directions, respectively. The turbine blade's pressure surface starts near the corner of the top boundary of the computational domain and ends approximately halfway from there to the outlet boundary. The suction surface of the blade sits in the same segment of the lower boundary of the computational domain. The portions of the top and bottom boundaries of the computational domain before and after the blade surfaces are aligned approximately with the freestreams of the flow, based on a computation using periodic boundary conditions of a turbine-blade cascade model. No periodic boundary conditions are used in this computation. The dimension perpendicular to the parallel side walls at the entrance is 0.06 m, which is identical to the inlet height of the class II curved channel. The centerline passes through the midpoint of the passage and has a total length of 0.286 m (2.6 times as long as that of the class II curved channel). The mixing layer enters the passage at an angle of 38 deg relative to the x axis. The inflow profiles and the boundary conditions are similar to those for the class II curved channel. Geometry causes the inlet Mach numbers and velocities for the turbinelike passage to differ from those for the class II curved channel with the same specified mass flow rate. The inflow conditions are given in Table 3. The Reynolds numbers at the inlet Re_δ are calculated from ΔU, δ_θ, and the mean viscosity.

Nonreacting and reacting mixing layers with the "FL" flow configuration are considered. This flow configuration was the one with the largest global chemical conversion rate among the class II curved cases. The nonreacting and reacting cases are identified as NFL-A-T and RFL-A-T, respectively, where the suffix "T" stands for the turbinelike passage. For all cases, a CFL number of 0.5 is used to ensure numerical stability.

Both the nonreacting and reacting mixing layers accelerate from low subsonic speed at the entrance to supersonic speed at the exit. For the nonreacting case (NFL-A-T), the time-averaged Mach number at the centerline near the exit is approximately 1.75; for the reacting case (RFL-A-T), the time-averaged Mach number at the centerline near the exit is approximately 1.7. The Mach numbers near the exit of the turbinelike passage are substantially higher than those for the
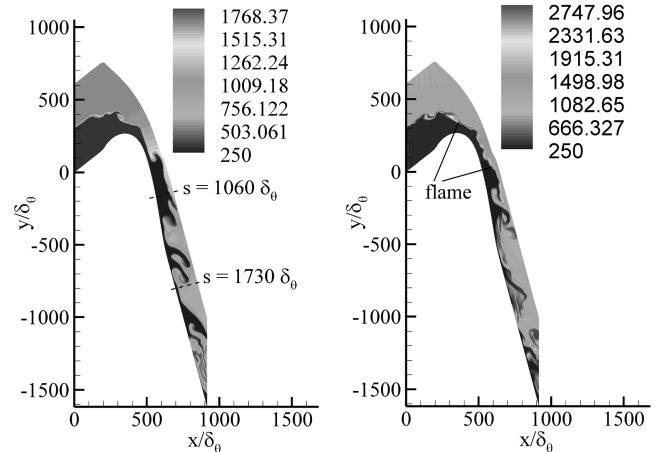
class II curved channel, due to the longer diverging section downstream of the channel throat. Also, the inlet Mach numbers are approximately 2 times higher in the turbinelike passage. The inflow velocities, channel length, and pressure gradient are quite different from those for the class II curved channel, making the quantitative comparison rather difficult; we instead focus on the qualitative aspects of the flow physics and compare the main features with the class II curved cases.

The instantaneous temperature fields for the NFL-A-T and RFL-A-T cases are shown in Figs. 17a and 17b, respectively. For both cases, the thicknesses of the mixing layers decrease in the converging portion (near the throat). This phenomenon was also observed in the class II curved case, in which the decrease in the thickness of the mixing layer was more pronounced because the class II channel converges at a greater rate. One major feature of the mixing layer is that the local cross section of the turbinelike passage can be intermittently occupied mostly by either the air or the fuel stream, due to the convergence of the passage and the unsteadiness. For example, in Fig. 17a, the turbinelike passage is occupied mostly by fuel at a streamwise location of $1060\delta_\theta$ and by air at a streamwise location of $1730\delta_\theta$. This feature also has a profound impact on the flame location. Because the mixing region of air and fuel can widely spread across the channel and can approach the side walls, the flame structures can traverse the channel and appear adjacent to the side walls, as shown in the figure. Similar phenomena were also captured in both class II straight and curved cases, but were absent in the class I cases, in which the channel transverse dimensions were constant and the streamwise gradients were imposed by varying the channel spanwise dimensions.

Another main feature of the reacting case in the turbinelike passage is the generation of vorticity layers of both signs. The instantaneous vorticity field for the RFL-A-T case is shown in Fig. 18; only part of the turbinelike passage near the throat is shown for better visualization. As indicated in the figure, the layer of positive vorticity lies on top of the layer of negative vorticity. The counter-rotating vortices are generated by the local streamwise velocity peak, due to the chemical reaction and streamwise acceleration.

From the observation of the temperature fields, both the NFL-A-T and RFL-A-T cases appear to be very unstable, and roll ups of the mixing layers occur near the inlet of the turbinelike passage. The

Table 3 Summary of the inflow conditions for the turbinelike passage (units of velocity, density, and temperature are m/s, kg/m³, and K, respectively)

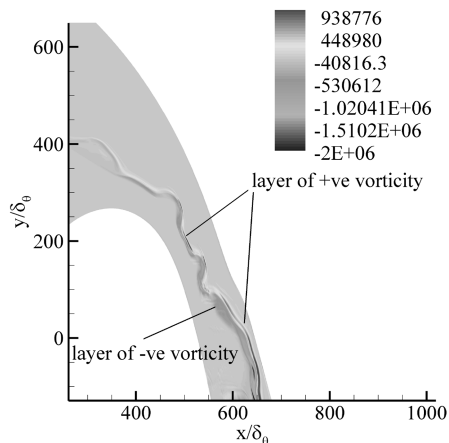|	Reaction	Vel. outside	Vel. inside	T outside	T inside	ρ outside	ρ inside	Re_δ
NFL-A-T	No	103.9	52.0	1650	300	1.07	3.22	862
RFL-A-T	Yes	97.8	48.9	1650	300	1.13	3.42	812

Fig. 18   Instantaneous contours of vorticity (1/s) for the RFL-A-T case in the turbinelike passage.
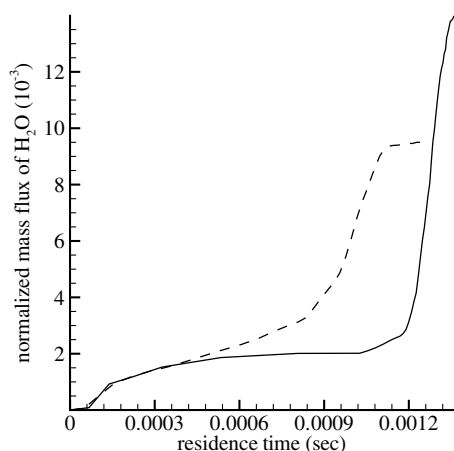

Fig. 19   Time-averaged mass flux of H_2O normalized by the total mass flux [case RFL-A-II (solid line), case RFL-A-T (dashed line)].

chemical conversion rates versus the residence times along the centerline are investigated in Fig. 19. Although the turbinelike passage has a longer length, the residence time is shorter because of the much higher flow speed. The chemical conversion rate for the RFL-A-T case increases steadily with time before it levels off at a residence time of about 0.0015 s. This time translates to spatial location of approximately $1280\delta_\theta$ or 56% of the total channel length. Within this period of time, the chemical conversion rate is more significant than that for the RFL-A-II case, due to the enhanced mixing of fluids. The saturation in the chemical conversion indicates flame extinction; it can be contributed by the stretching of the flame structure due to the acceleration and the lowered temperature associated with the expansion. For the RFL-A-II case, the residence time at 0.0012 s translates to a streamwise location of approximately $300\delta_\theta$. The chemical conversion rate increases rapidly beyond that point because the mixing is much enhanced due to the development of large unstable structures (see Fig. 13).

VI.   Conclusions

Mixing layers in the straight and curved channels with converging–diverging side walls have been investigated. The streamwise pressure gradient is imposed by contracting and expanding the channel dimension in the y direction of the x–y plane, while keeping the channel span in the z direction constant. The thickness of the mixing layer decreases as the flow passes through the sharply converging section. The reduced thickness results in larger transverse gradients in flow properties and more concentrated vorticity. For both the straight and curved cases, the mixing layers are much more unstable than the corresponding cases in the channel with

constant transverse dimension [17]; the enhanced instability was contributed by the more concentrated vorticity. The converging–diverging side walls also had profound effects on the combustion. The global chemical conversion rate is much larger than that for the corresponding reacting case in the channel with constant transverse dimension, due to the enhanced mixing of the fluids. Consistent with the previous finding [16,17], the reacting mixing layer is always more unstable than its nonreacting counterpart. One major feature of the flow is that the channel cross section can be intermittently occupied mostly by either the air or fuel stream, due to the convergence of the channel and unsteadiness. This phenomenon was not observed in the channel with constant transverse dimension.

The curved mixing layers passing through a two-dimensional turbinelike passage have also been studied. Although the flow variables and the geometry for the turbinelike passage are quite different from those for the class II curved channel, the qualitative aspects of the flow are similar. The major features of the flow, such as the effects of the converging side walls on the development of the mixing layer, the generation of counter-rotating vortices, and the destabilizing effects of the chemical reactions, were also captured in the class II curved channel.

Finally, the present 2-D numerical simulation is recommended to be extended to three dimensions in future studies. In a 3-D simulation, the omitted effects, such as the 3-D instability mode for the straight mixing layer and the 3-D mechanisms associated with the centrifugal, R-T, and Görtler instabilities for the curved mixing layer, can be captured. These instability modes induce streamwise vortical structures that may dominate the development of the mixing layer in the fully turbulent regime. Future studies will provide fundamental understanding of the 3-D aspects of the mixing layer and more practical guidance to the design of the turbine burner.

Acknowledgment

References

[1] Sirignano, W. A., and Liu, F., "Performance Increases for Gas-Turbine Engines Through Combustion Inside the Turbine," *Journal of Propulsion and Power*, Vol. 15, No. 1, 1999, pp. 111–118. doi:10.2514/2.5398

[2] Liu, F., and Sirignano, W. A., "Turbojet and Turbofan Engine Performance Increases Through Turbine Burners," *Journal of Propulsion and Power*, Vol. 17, No. 3, 2001, pp. 695–705. doi:10.2514/2.5797

[3] Sirignano, W. A., and Kim, I., "Diffusion Flame in a Two-Dimensional, Accelerating Mixing Layer," *Physics of Fluids*, Vol. 9, No. 9, 1997, pp. 2617–2630. doi:10.1063/1.869378

[4] Fang, X., Liu, F., and Sirignano, W. A., "Ignition and Flame Studies for an Accelerating Transonic Mixing Layer," *Journal of Propulsion and Power*, Vol. 17, No. 5, 2001, pp. 1058–1066. doi:10.2514/2.5844

[5] Mehring, C., Liu, F., and Sirignano, W. A., "Ignition and Flame Studies for an Accelerating Transonic Turbulent Mixing Layer," AIAA Paper 01-0190, 2001.

[6] Cai, J., Icoz, O., Liu, F., and Sirignano, W. A., "Ignition and Flame Studies for Turbulent Transonic Mixing Layer in a Curved Duct Flow," AIAA Paper 01-0180, 2001.

[7] Ho, C. M., and Huerre, P., "Perturbed Free Shear Layers," *Annual Review of Fluid Mechanics*, Vol. 16, Jan. 1984, pp. 365–424. doi:10.1146/annurev.fl.16.010184.002053

[8] Winant, C. D., and Browand, F. K., "Vortex Pairing: The Mechanism of Turbulent Mixing Layer Growth at Moderate Reynolds Number," *Journal of Fluid Mechanics*, Vol. 63, No. 2, 1974, pp. 237–255. doi:10.1017/S0022112074001121

[9] Rogers, M. M., and Moser, R. D., "The Three-Dimensional Evolution of a Plane Mixing Layer: the Kelvin-Helmholtz Rollup," *Journal of Fluid Mechanics*, Vol. 243, Oct. 1992, pp. 183–226. doi:10.1017/S0022112092002696

[10] Moser, R. D., and Rogers, M. M., "The Three-Dimensional Evolution of a Plane Mixing Layer: Pairing and Transition to Turbulence,"

Journal of Fluid Mechanics, Vol. 247, Feb. 1993, pp. 275–320.
doi:10.1017/S0022112093000473

[11] Drazin, P. G., and Reid, W. H., *Hydrodynamic Stability*, Cambridge Univ. Press, Cambridge, England, U.K., 1981.

[12] Loiu, W. W., "Linear Stability of Curved Free Shear Layers," *Physics of Fluids*, Vol. 6, No. 2, 1994, pp. 541–549.
doi:10.1063/1.868350

[13] Zhuang, M., "The Effects of Curvature on Wake-Dominated Incompressible Free Shear Layers," *Physics of Fluids*, Vol. 11, No. 10, 1999, pp. 3106–3115.
doi:10.1063/1.870168

[14] Shin, D. S., and Ferziger, J. H., "Linear Stability of the Reacting Mixing Layer," *AIAA Journal*, Vol. 29, No. 10, 1991, pp. 1634–1642.
doi:10.2514/3.10785

[15] Shin, D. S., and Ferziger, J. H., "Linear Stability of the Compressible Reacting Mixing Layer," *AIAA Journal*, Vol. 31, No. 4, 1993, pp. 677–685.
doi:10.2514/3.11603

[16] Cheng, F., Sirignano, W. A., and Liu, F., "Nonpremixed Combustion in an Accelerating Transonic Flow Undergoing Transition," *AIAA Journal*, Vol. 45, No. 12, 2007, pp. 2935–2948.
doi:10.2514/1.31146

[17] Cheng, F., Sirignano, W. A., and Liu, F., "Nonpremixed Combustion in an Accelerating Turning Transonic Flow Undergoing Transition," *AIAA Journal*, Vol. 46, No. 5, 2008, pp. 1204–1215.
doi:10.2514/1.35209

[18] Westbrook, C. K., and Dryer, F. L., "Chemical Kinetic Modeling of Hydrocarbon Combustion," *Progress in Energy and Combustion Science*, Vol. 10, No. 1, 1984, pp. 1–57.
doi:10.1016/0360-1285(84)90118-7

[19] White, F. M., *Viscous Fluid Flow*, 2nd. ed., McGraw–Hill, New York, 1991.

[20] Steger, J. L., and Warming, R. F., "Flux Vector Splitting of the Inviscid Gasdynamic Equations with Application to Finite-Difference Methods," *Journal of Computational Physics*, Vol. 40, No. 2, 1981, pp. 263–293.
doi:10.1016/0021-9991(81)90210-2

[21] Hirsch, C., Numerical Computation of Internal and External Flows, *Computational Methods for Inviscid and Viscous Flows*, Vol. 2, Wiley, New York, 1990.

[22] Poinsot, T. J., and Lele, S. K., "Boundary Conditions for Direct Simulations of Compressible Viscous Flows," *Journal of Computational Physics*, Vol. 101, No. 1, 1992, pp. 104–129.
doi:10.1016/0021-9991(92)90046-2

[23] Grinstein, F. F., "Open Boundary Conditions in the Simulation of Subsonic Turbulent Shear Flows," *Journal of Computational Physics*, Vol. 115, No. 1, 1994, pp. 43–55.
doi:10.1006/jcph.1994.1177

[24] Grinstein, F. F., Oran, E. S., and Boris, J. P., "Pressure Field, Feedback, and Global Instabilities of Subsonic Spatially Developing Mixing Layers," *Physics of Fluids A*, Vol. 3, No. 10, 1991, pp. 2401–2409.
doi:10.1063/1.858178

[25] Monkewitz, P. A., and Huerre, P., "Influence of the Velocity Ratio on the Spatial Instability of Mixing Layers," *Physics of Fluids*, Vol. 25, No. 7, 1982, pp. 1137–1143.
doi:10.1063/1.863880

[26] Groppengiesser, H., "Study on the Stability of Boundary Layers in Compressible Fluids," NASA TT F-12, 1970.

C. Segal
Associate Editor